

■ Hydrogen Evolution Reaction



Platinum Oxide Nanoparticles for Electrochemical Hydrogen Evolution: Influence of Platinum Valence State

Forrest Nichols,^[a] Jia En Lu,^[a] Rene Mercado,^[a] Ryan Dudschus,^[b] Frank Bridges,^[b] and Shaowei Chen^{*[a]}

Abstract: Electrochemical hydrogen generation is a rising prospect for future renewable energy storage and conversion. Platinum remains a leading choice of catalyst, but because of its high cost and low natural abundance, it is critical to optimize its use. In the present study, platinum oxide nanoparticles of approximately 2 nm in diameter are deposited on carbon nitride (C₃N₄) nanosheets by thermal refluxing of C₃N₄ and PtCl₂ or PtCl₄ in water. These nanoparticles exhibit apparent electrocatalytic activity toward the hydro-

gen evolution reaction (HER) in acid. Interestingly, the HER activity increases with increasing Pt⁴⁺ concentration in the nanoparticles, and the optimized catalyst even outperforms commercial Pt/C, exhibiting an overpotential of only −7.7 mV to reach the current density of 10 mA cm^{−2} and a Tafel slope of −26.3 mV dec^{−1}. The results from this study suggest that the future design of platinum oxide catalysts should strive to maximize the Pt⁴⁺ sites and minimize the formation of the less active Pt²⁺ species.

Introduction

It has been proposed that 80% of the electricity generated in the United States has the potential to be made renewable by 2050.^[1] With the prospect of completely renewable electricity on the horizon, electrochemical water splitting for hydrogen generation provides a promising technology for sustainable energy storage and conversion.^[2,3] However, implementation of this technology will require improved catalyst design.^[4] Platinum has remained a leading electrocatalyst for the multi-electron-transfer process of the hydrogen evolution reaction (HER), with a high exchange-current density and ideal Tafel slope.^[5] However, owing to the high cost and low natural abundance of platinum, future catalysts must optimize the use of platinum within the materials.^[6,7] To achieve this goal, researchers have developed various methods to limit the amount of platinum by reducing particle size, and by using platinum oxide rather than platinum metal particles. For instance, Yang et al. used platinum oxide nanoparticles for HER catalysis and found that decreasing the particle size from 2 to 0.2 nm resulted in increased catalytic activity, which was attributed to size-depend-

ent proton adsorption properties.^[8] More recently, Sarno and colleagues showed that decreasing particle size as well as strong metal oxide–support interactions can help reduce platinum loading and improve hydrogen evolution rates by using a composite material containing platinum metal, platinum(IV) oxide, and iron oxide.^[9] Strong metal–support interactions were also reported by Cheng et al., who used platinum oxide clusters containing Pt²⁺ and Pt⁴⁺ species supported on TiO₂.^[10] It is widely believed that hydrogen adsorption onto the catalyst surface, known as the Volmer step, is often the rate-determining step for the HER in both acidic and basic media.^[11,12] Therefore, to better understand the reaction rates, Cheng and colleagues used density functional theory (DFT) to calculate changes in Gibbs free energy (ΔG_{H}) for hydrogen adsorption. It was found that platinum in a highly oxidized state resulted in a ΔG_{H} value close to zero (−0.06 eV), which is ideal for the HER. This improved hydrogen binding was attributed to the presence of Pt⁴⁺ sites in Pt–O–Ti bonding. This result suggests that highly oxidized platinum sites can adsorb hydrogen efficiently onto the surface, but also minimize the adsorption energy to allow for hydrogen gas formation and release from the catalyst surface. However, the material under study^[10] contained a large portion of platinum in a lower oxidation state (Pt²⁺), and the HER performance remained subpar compared with that of commercial Pt/C. In addition, the catalytic contributions and importance of the portion of low-valence platinum were not distinguished. Therefore, further study is required to understand how the oxidation state of platinum can be controlled to tailor the hydrogen evolution performance. With this in mind, controlling the platinum oxidation state within the oxide material poses a useful route to effective catalyst design.

[a] F. Nichols, Dr. J. E. Lu, R. Mercado, Prof. S. W. Chen
Department of Chemistry and Biochemistry, University of California
1156 High Street, Santa Cruz, California 95064 (USA)
E-mail: shaowei@ucsc.edu

[b] R. Dudschus, Prof. F. Bridges
Department of Physics, University of California
1156 High Street, Santa Cruz, California 95064 (USA)

 Supporting information and the ORCID identification number(s) for the author(s) of this article can be found under:
<https://doi.org/10.1002/chem.201904559>

 Part of a Special Issue on Electrocatalysis: Mechanism and Applications. To view the complete issue, visit Issue 18, 2020.

The selection of an ideal catalyst support is also critical as this plays a key role in the manipulation of the resulting particle size, stability, and other key factors influencing the catalytic performance.^[13–15] Graphitic carbon nitride (C3N4) represents a promising support because of its surface functionality, ease and low cost of production, and inherent ability to control nanoparticle size. Zhu and colleagues have shown how the manipulation of C3N4 condensation rate and temperature can be used to control the size of the resulting gold and platinum nanoparticles in a C3N4-mesoporous silica (SBA-15) composite material.^[16] It was shown that incorporation of C3N4 resulted in small, homogeneously dispersed nanoparticles and prevented nanoparticle agglomeration, which was attributed to strong support interactions, in contrast to SBA-15 alone. Vinu and co-workers demonstrated the inherent ability of C3N4 to act as a stabilizing agent to produce ultrasmall, highly dispersed Au nanoparticles anchored firmly on the functional moieties on the C3N4 surface. This can be attributed to the pyridinic nitrogen atoms on the C3N4 surface, which act as a strong Lewis base and form π -bond planar layers that are able to anchor and stabilize the nanoparticles.^[17] For these reasons, C3N4 is an ideal candidate for the fabrication of small metal oxide nanoparticle composites.

Herein, we report a facile, effective approach to properly distinguish contributions from different platinum oxide species toward the HER, utilizing C3N4 as a unique support material. C3N4 nanosheets are first prepared by condensation of urea through a two-step route. Platinum oxide nanoparticles of about 2.0 nm in diameter are then grown onto the C3N4 surface by a thermal refluxing method in water with platinum chloride.^[18–20] Electrochemical measurements show that the Pt⁴⁺ species is primarily responsible for the remarkable HER activity, which even surpasses that of commercial Pt/C, and that the HER activity increases with increasing Pt⁴⁺ content.

Results and Discussion

The C3N4 nanosheets were prepared by thermal treatment of urea; then, platinum oxide nanoparticles were deposited on the nanosheets by thermal refluxing of C3N4 and PtCl₂ or PtCl₄ in water at 90 °C. The resulting samples are referred to as Pt2+90C and Pt4+90C (synthetic details in the Experimental Section). Figure 1 depicts representative TEM images of a) Pt2+90C and b) Pt4+90C (additional TEM data shown in Figure S1, Supporting Information). The overall morphologies are consistent with those of the as-prepared C3N4 (Figure S2, Supporting Information), displaying a layered, sheet-like structure. In addition, both the Pt2+90C and Pt4+90C samples are seen to contain a number of dark-contrast nanoparticles deposited on the C3N4 surface (note that no such nanoparticulate objects were observed in the C3N4 sample, Figure S2). From the core histograms in Figure S3 (Supporting Information), the nanoparticles can be seen to fall mostly within the narrow range of 1.0–4.4 nm, with an average particle diameter of 2.0 ± 0.6 nm for Pt2+90C and 2.1 ± 0.7 nm for Pt4+90C. Furthermore, high-resolution TEM images reveal clearly defined lattice fringes of the nanoparticles (insets to Figure 1), with an

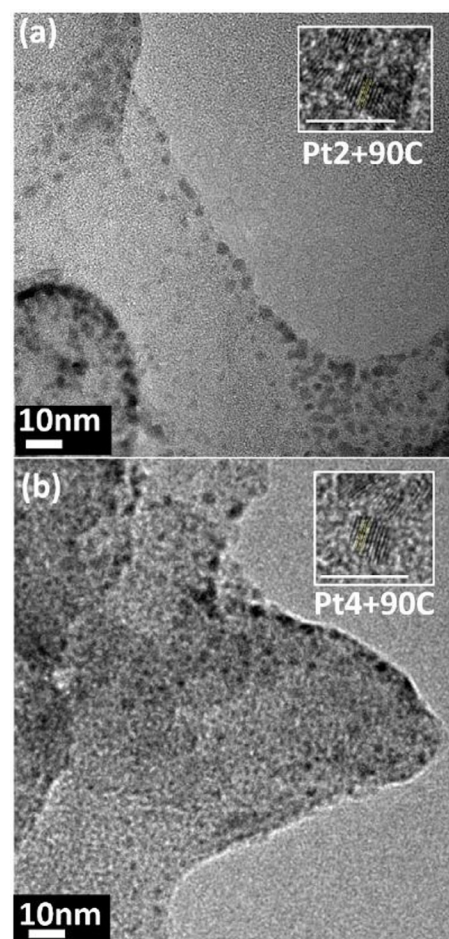


Figure 1. TEM images of a) Pt2+90C and b) Pt4+90C. Scale bars 10 nm. Insets are the corresponding high-resolution TEM images, with scale bars of 5 nm.

interplanar spacing of 0.23 nm for Pt2+90C and 0.24 nm for Pt4+90C, which are consistent with several crystalline facets, such as PtO(110), PtO₂(011), and Pt(111).^[21,22] However, the further characterizations described below suggest that these are actually attributable to the formation of platinum oxide PtO_x (vide infra).

Further structural insights were obtained in X-ray diffraction (XRD) measurements. From Figure S4 (Supporting Information), it is seen that Pt4+90C, Pt2+90C, and C3N4 all exhibit a single, major diffraction peak centered at $2\theta = 27^\circ$, which can be assigned to the (002) crystalline facets of carbon nitride, as observed previously.^[23] In the Pt4+90C and Pt2+90C samples, the diffraction patterns of platinum oxide cannot be resolved in comparison with the standard references of PtO (reference code 00-027-1331) and PtO₂ (reference code 01-075-0978), probably because of the small nanoparticle size, as seen from the TEM measurements (Figure 1 and Figure S1).

XPS measurements were then performed to probe the chemical composition and electronic environment of the materials. From the survey spectra in Figure 2a, two major peaks can be seen at 288 and 399 eV, attributed to the C 1s and N 1s electrons of C3N4, respectively. For Pt2+90C and Pt4+90C,

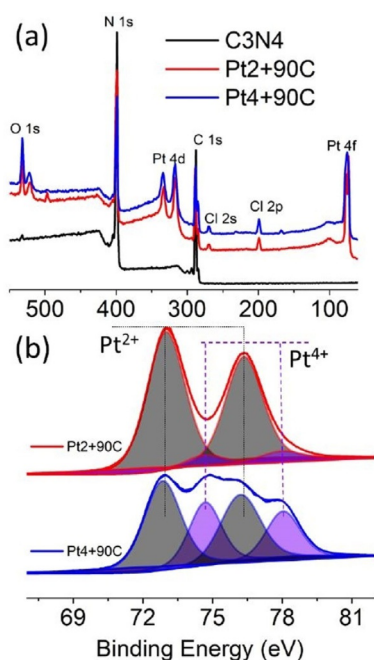


Figure 2. a) XPS survey spectra of as-prepared C3N4 (black), Pt2+90C (red), and Pt4+90C (blue). b) High-resolution scans of the Pt 4f electrons of Pt2+90C (top) and Pt4+90C (bottom). Solid curves are experimental data and shaded peaks are deconvolution fits.

two additional species can be identified at around 75 eV for Pt4f,^[24] and 532 eV for O1s, indicating the successful deposition of platinum species onto the C3N4 surface (the small peaks at 199 and 270 eV can be assigned to Cl2p and Cl2s, respectively, owing to residual chloride in the samples).^[25] On the basis of the integrated peak areas, the Pt loadings were found to be very comparable, at 32 wt% for Pt4+90C and 28 wt% for Pt2+90C. Figure 2b depicts the corresponding high-resolution XPS scans of the Pt4f electrons. The Pt2+90C sample (red curve) exhibits two doublets. The first pair at 76.35 and 73.00 eV corresponds to the 4f_{5/2} and 4f_{7/2} electrons of Pt²⁺, whereas the other at 78.05 and 74.70 eV is attributed to those of Pt⁴⁺, and a peak splitting of 3.35 eV is consistent with Pt4f spin-orbit coupling (note that no metallic Pt can be resolved).^[9,20,24,26,27] Additionally, on the basis of the integrated peak areas, the atomic ratio of Pt⁴⁺/Pt²⁺ in Pt2+90C is estimated to be 0.06:1. Similar behaviors can be seen with the Pt4+90C sample, for which the two doublets appear at 76.20/72.85 eV and 78.04/74.69 eV, respectively. However, the ratio of Pt⁴⁺/Pt²⁺ is significantly higher at 0.6:1, 10 times that in Pt2+90C. Nevertheless, this suggests that thermal refluxing of platinum chloride and C3N4 effectively led to the deposition of PtO_x nanoparticles onto the C3N4 surface (Figure 1).

The high-resolution scans of the C1s and N1s electrons are depicted in Figure S5 (Supporting Information). Deconvolution reveals two distinct peaks at 287.85 and 284.33 eV for the C3N4 sample, which are attributed to the sp²-hybridized carbon within the C3N4 network (C–N=C) and sp³ carbon from defect moieties (C–C), respectively.^[23,28–30] The N1s region of C3N4 was deconvoluted into four components centered at 398.34, 399.81, 400.96 eV, and a weak one at 404.10 eV. These

individual components can be attributed to the sp²-hybridized pyridinic nitrogen (C–N=C), sp³-hybridized tertiary nitrogen (N–(C)₃), quaternary nitrogen (C–N–H), and a π-satellite excitation, respectively.^[23,28–30] Upon thermal refluxing with platinum salts, the nitrogen and carbon peaks associated with the C3N4 matrix exhibit an increase in binding energy. The primary carbon peak shifts to 287.97 and 288.04 eV (C–N=C), and the defect carbon to 284.53 and 284.57 eV (C–C) for Pt2+90C and Pt4+90C, respectively. The N1s electrons also experience a similar increase in binding energy, with the three primary peaks centered at 398.47 and 398.54 eV (C–N=C), 399.92 and 399.88 eV (N–(C)₃), and 401.10 and 401.18 eV (C–N–H), again corresponding to Pt2+90C and Pt4+90C, respectively. This slight increase in binding energy can be attributed to electron donation from the C3N4 support to the Pt centers, suggesting a strong interaction between the nanoparticles and C3N4.^[31,32]

Further structural insights were obtained in X-ray absorption spectroscopic (XAS) measurements, in which data were collected at the Pt L3 edge to probe the Pt electronic states and investigate the local structures. The data were reduced and analyzed using the REXAP package.^[33] In Figure 3a, the Pt L3 XANES (X-ray absorption near edge spectroscopy) data for

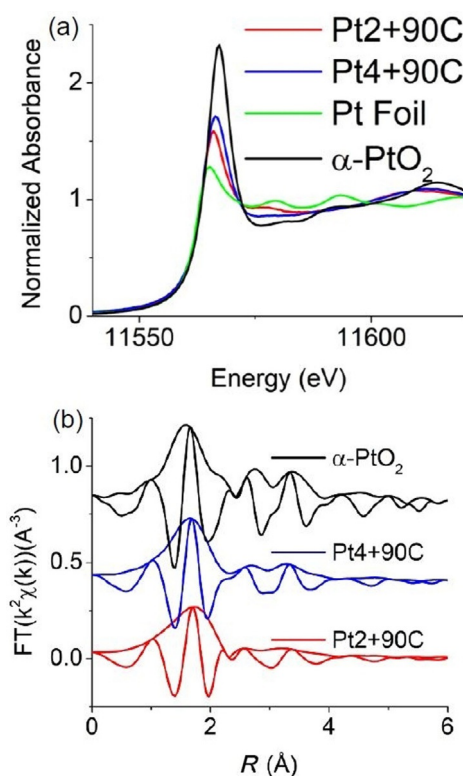


Figure 3. a) Pt L3 edge XANES data for Pt2+90C and Pt4+90C (Pt foil and commercial α-PtO₂ as references). All edge steps are normalized to an edge step height of 1. The energy range selected to normalize the edge is 11700–12000 eV. Measurements were performed at the temperature of 10 K. b) Pt L3 edge r-space data for Pt2+90C (red), Pt4+90C (blue), and commercial α-PtO₂ (black). The Fourier transform (FT) window is from 3.0 to 10.8 Å⁻¹, rounded using a Gaussian function of width, 0.2 Å⁻¹. The fast oscillating function is the real part R of the FT, and the amplitude is (R²+I²)^{1/2}, in which I is the imaginary part of the FT. Pt4+90C has been shifted vertically by 0.4, and α-PtO₂ has been shifted vertically by 0.8.

Pt2+90C and Pt4+90C are compared with those for a Pt foil and the α -PtO₂ reference sample. All samples are electrically conducting and there is no shift of the main edge as typically observed for different valences in insulating materials, suggesting that the Fermi energies are nearly identical between the samples. A strong absorption in this region, referred to as the white line, is observed and attributed to the Pt 2p→5d transitions.^[34,35] Typically, the white line intensity increases with decreasing 5d orbital occupancy (i.e., increasing valence states).^[35–37] The white line intensity increases in the order Pt foil < Pt2+90C < Pt4+90C < PtO₂, indicating that the Pt charge state in Pt2+90C and Pt4+90C fell in the intermediate range between Pt⁰ and Pt^{IV}, and is higher in Pt4+90C than in Pt2+90C, in good agreement with the results of XPS measurements (Figure 2). Consistent behaviors can be seen with the white line energy, which shifts positively in the order Pt foil (11 565.16 eV) < Pt2+90C (11 566.00 eV) < Pt4+90C (11 566.44 eV) < α -PtO₂ (11 567.27 eV).

EXAFS (extended X-ray absorption fine structure) analysis for Pt2+90C and Pt4+90C was then performed, and the results compared with those for α -PtO₂ in Figure 3b. The same FT range (3.0 to 10.8 Å⁻¹) is used for each plot, although the k-space data for α -PtO₂ extend to much higher k (Figure S6, Supporting Information). The k-space plots show increasing disorder from the reference sample to Pt2+90C. Note that the double peak structure near 3 Å in Figure 3b, associated with Pt–Pt second neighbor pairs in α -PtO₂, is nearly washed out for the latter sample. α -PtO₂ has a hexagonal structure,^[38,39] and the environment around Pt consists of six nearest-neighbor O atoms, six second-neighbor Pt atoms, and six third-neighbor O atoms. To fit the data, theoretical Pt–O and Pt–Pt functions were calculated for α -PtO₂ using FEFF7,^[40] plus a weak multiscattering peak. As shown in Figure 4, the data were then fitted to a sum of such standards, allowing the pair distances and pair distribution widths, σ , to vary. Note that the third-neighbor Pt–O₂ and the multiscattering peak amplitudes are very small, and we only quote the results for the first two neighbors. As shown in Table 1, the Pt–O bond length is somewhat shorter for Pt4+90C than for Pt2+90C. A similar change is also observed for the second neighbors, again consistent with a higher charge state of Pt in Pt4+90C than in Pt2+90C.

To assess the electrocatalytic performance of these materials toward the HER, linear sweep voltammetry was performed under a nitrogen atmosphere in 0.5 M H₂SO₄ at the potential scan rate of 10 mV s⁻¹. Figure 5a displays the polarization curves of Pt2+90C, Pt4+90C, and commercial Pt/C, in comparison with that of C3N4. It is seen that C3N4 exhibited essentially zero HER activity, whereas apparent catalytic activity appears with the other three Pt-containing samples. Remarkably, at equivalent platinum mass loadings, Pt4+90C stood out as the best among the series, even outperforming commercial Pt/C, with an ultralow overpotential (η_{10}) of only -7.7 mV to reach the current density of 10 mA cm⁻², compared with -26.1 mV for Pt/C and -214.6 mV for Pt2+90C, suggesting that the Pt⁴⁺ species played a critical role in the HER activity. To the best of our knowledge, the Pt4+90C sample outperforms most platinum-oxide-based HER catalysts in acidic media

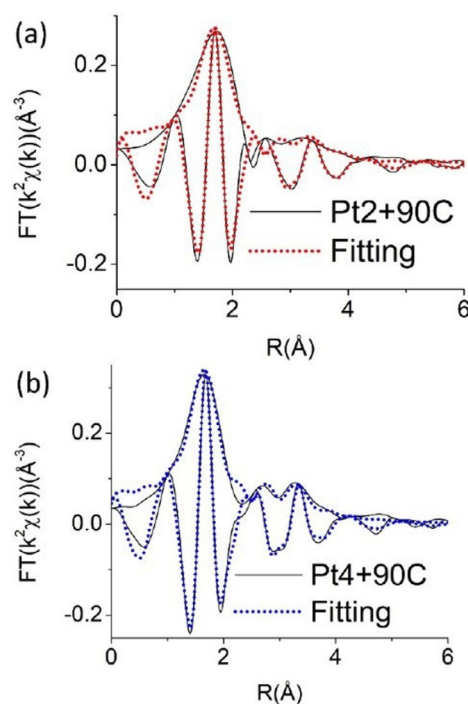


Figure 4. Fittings to the hexagonal structure of α -PtO₂, as a sum of Pt–O and Pt–Pt, for a) Pt2+90C and b) Pt4+90C. Pt–O bond length decreases from 2.07 to 2.03 Å.

Table 1. EXAFS fitting results to hexagonal α -PtO₂.

Sample	Pt–O [Å]	Pt–Pt [Å]
Pt2+90C	2.071 ± 0.01	3.204 ± 0.02
Pt4+90C	2.034 ± 0.01	3.154 ± 0.02

that have been reported in recent literature (Table S1, Supporting Information). For further understanding of the reaction mechanisms of these materials, Tafel plots were derived from the polarization curves, as shown in Figure 5b, from which the Tafel slopes were estimated to be 21.0, 26.3, and 55.4 mV dec⁻¹ for Pt/C, Pt4+90C and Pt2+90C, respectively.^[41] This suggests that kinetically, Pt4+90C behaved similarly to Pt/C, whereby the Tafel reaction is the rate-determining step, whereas for Pt2+90C, the HER is probably limited by the slower Heyrovsky reaction.

Figure S7 (Supporting Information) depicts the Nyquist plots (squares) and the corresponding fits (solid lines) using a typical Randle's equivalent circuit modified with a Warburg diffusion term (W2). The charge-transfer resistance (R_{CT}) was estimated to be 2230 Ω for the as-prepared C3N4, and diminished markedly to 26.8 Ω for Pt2+90C, and only 1.6 Ω for Pt4+90C. That is, the charge-transfer kinetics of the HER were improved dramatically with the deposition of platinum onto C3N4, and the Pt4+90C sample showed the lowest charge-transfer resistance among the series of samples.

To examine further the influence of the Pt oxidation state on the HER performance, we performed several additional electrochemical measurements. In the first test, the Pt2+90C sample

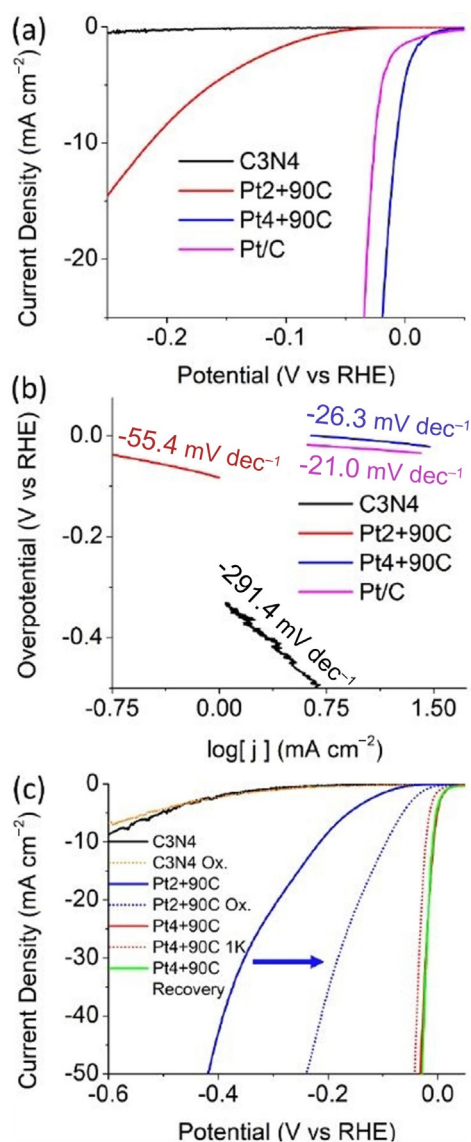


Figure 5. a) Polarization curves of HER in 0.5 M H_2SO_4 for as prepared C3N4 (black), Pt2+90C (red), Pt4+90C (blue), and commercial platinum on carbon (magenta). b) Tafel plots derived from polarization curves in panel (a). c) Oxidized cycling and recovery tests.

was found to show a marked improvement in HER performance after 50 cycles at high potentials between +0.9 and +1.2 V versus RHE (in which Pt^{2+} was oxidized electrochemically to Pt^{4+}) at the potential scan rate of 50 mV s^{-1} . From Figure 5c, it is seen that η_{10} diminished drastically by almost 120 to -93.8 mV (blue solid and dotted curves). XPS measurements (Figure S8, Supporting Information) show that the primary peak appears at 73.86 eV, approximately 0.9 eV higher than that of the as-prepared sample, suggesting the formation of Pt^{4+} species, which led to the improved HER performance.^[9,20,24,26,27] Additional tests were performed with the Pt4+90C sample. The catalyst was subjected to potential cycling between 0 and -0.02 V versus RHE (in which Pt^{4+} was reduced electrochemically to lower valence states) for 1000 cycles at 10 mV s^{-1} , and the η_{10} value in the subsequent HER measurement was found to deteriorate slightly from -7.7

to -21.7 mV (red solid and dotted curves). However, after 50 potential cycles between +0.9 and +1.2 V to regenerate the Pt^{4+} species, the HER performance was almost fully recovered, with $\eta_{10} = -9.8 \text{ mV}$ (green solid curve). In sharp contrast, electrochemical treatment (reduction or oxidation, black solid and orange dotted curves) of C3N4 alone did not lead to any change in the electrochemical response, suggesting that it is the Pt species that are responsible for the HER activity, and that Pt^{4+} is far more active than Pt^{2+} . Indeed, the HER activity increased markedly with increasing Pt^{4+} loading in the Pt4+90C sample (Figure S9, Supporting Information).

Conclusions

In summary, PtO_x nanoparticles were deposited onto C3N4 surfaces by thermal refluxing of C3N4 nanosheets and platinum chloride in water. The nanocomposites displayed similar platinum loading and particle size, but with stark differences in the platinum valence states. It was shown that the platinum oxidation state greatly influenced the hydrogen evolution performance under electrochemical conditions, and platinum oxide nanoparticles primarily in the 4+ charge state exhibited HER performance superior even to that of commercial platinum on carbon in acid media. This catalyst showed excellent recoverability after recycling the material under oxidizing conditions. Results from the present study suggest that the future design of platinum oxide catalysts should attempt to optimize the valence states of platinum by minimizing the formation of the less oxidized and less active species.

Experimental Section

Chemicals

Urea (Certified ACS, Fisher Chemicals), platinum(II) chloride (PtCl_2 , 73% Pt, ACROS Organics), platinum(IV) chloride (PtCl_4 , 99%, ACROS Organics), platinum on carbon (Pt/C, nominally 20 wt%, Alfa Aesar), platinum(IV) oxide ($\alpha\text{-PtO}_2$, Matheson Coleman & Bell), carbon black (Vulcan XC 72R), and Nafion 117 (Sigma-Aldrich) were used as received. All solvents were obtained through typical commercial sources and used as received. Water was supplied from a Barnstead Nanopure water system ($18.3 \text{ M}\Omega \text{ cm}$).

Synthesis of graphitic carbon nitride

Graphitic carbon nitride (C3N4) was prepared by adopting a method reported previously.^[23,28] Briefly, urea (15 g) was placed in a crucible, covered, heated in air to 300°C at a rate of 2°C min^{-1} , and held for 3 h. The resulting white solid was ground to a fine powder, heated again in air to 520°C at a rate of $20^\circ\text{C min}^{-1}$, and held for 4 h. The resulting light yellow solid was collected and washed with Nanopure water, filtered, and dried in a vacuum furnace for 24 h at 60°C , affording C3N4.

Synthesis of platinum oxide on graphitic carbon nitride

Platinum oxide deposition was performed by following a method described previously.^[8,20] Briefly, C3N4 (50 mg, prepared as described above) was dispersed in Nanopure water (50 mL) under ultrasonication for 1 h. The resulting dispersion was then placed

onto a hot plate under stirring. PtCl₂ or PtCl₄ (0.27 mmol) was added slowly to the stirring solution and allowed to mix at 90 °C for 48 h. In the case of PtCl₂, the salt was first dissolved in HCl and neutralized with anhydrous sodium carbonate to achieve a neutral pH before addition. The products were collected by centrifugation at 4500 rpm for 10 min, washed with Nanopure water and acetone, and dried in a vacuum oven overnight; they were named Pt2+90C and Pt4+90C. It should be noted that the supernatant exhibited an orange color, indicative of an excess of platinum chloride in the solution, and became clear after washing, signifying the effective removal of excess metal salts.

Characterization

TEM measurements were performed on a JOEL JEM 2100F microscope. XRD patterns were acquired with a Bruker D8 Advance diffractometer with CuK_α radiation ($\lambda=0.15418$ nm). XPS measurements were performed with a Phi 5400/XPS instrument equipped with an AlK_α source operated at 350 W and 10⁻⁹ torr. XAS measurements were performed at 10 K on beamline 4-1 at the Stanford Synchrotron Radiation Lightsource using an Oxford liquid helium cryostat.

Electrochemistry

Electrochemical measurements were performed with a CHI710 workstation, and electrochemical impedance measurements were carried out with a Gamry Reference 600 instrument. A glassy carbon electrode (5.60 mm in diameter, 0.246 cm²) was used as the working electrode, and a Ag/AgCl (1.0 M KCl) electrode and graphite rod were used as the reference and counter electrodes, respectively. The Ag/AgCl electrode was calibrated versus a reversible hydrogen electrode (RHE), and all potentials in the present study were referenced to this RHE. In a typical experiment, a dry sample prepared above (2 mg) was mixed with carbon black (3 mg) and sonicated for 20 min in isopropanol (1 mL); this was followed by addition of Nafion (40 μ L) and sonication for an additional 10 min. The prepared ink (30 μ L) was dropped onto the surface of the glassy carbon electrode and dried at room temperature, corresponding to a catalyst mass loading of 0.244 mg cm⁻².

Acknowledgements

This work is supported, in part, by the National Science Foundation (CHE-1710408 and CHE-1900235). TEM and XPS work was undertaken at the National Center for Electron Microscopy and Molecular Foundry of Lawrence Berkeley National Laboratory, which is supported by the US Department of Energy, as part of a user project. XAS experiments were performed at the Stanford Synchrotron Radiation Lightsource (SSRL), which is also supported by the US Department of Energy.

Conflict of interest

The authors declare no conflict of interest.

Keywords: carbon nitride · electrochemistry · nanoparticles · platinum oxide · valence state

- [1] *Renewable Electricity Futures Study, Vol. 1–4* (Eds.: M. M. Hand, S. Baldwin, E. DeMeo, J. M. Reilly, T. Mai, D. Arent, G. Porro, M. Meshek, D. Sandor), National Renewable Energy Laboratory, Golden, **2012**.
- [2] J. Greeley, T. F. Jaramillo, J. Bonde, I. B. Chorkendorff, J. K. Nørskov, *Nat. Mater.* **2006**, *5*, 909–913.
- [3] D. Voiry, H. Yamaguchi, J. W. Li, R. Silva, D. C. B. Alves, T. Fujita, M. W. Chen, T. Asefa, V. B. Shenoy, G. Eda, M. Chhowalla, *Nat. Mater.* **2013**, *12*, 850–855.
- [4] M. Cabán-Acevedo, M. L. Stone, J. R. Schmidt, J. G. Thomas, Q. Ding, H.-C. Chang, M.-L. Tsai, J.-H. He, S. Jin, *Nat. Mater.* **2015**, *14*, 1245.
- [5] A. Eftekhari, *Int. J. Hydrogen Energy* **2017**, *42*, 11053–11077.
- [6] C. Sealy, *Mater. Today* **2008**, *11*, 65–68.
- [7] Z. P. Zhao, H. T. Liu, W. P. Gao, W. Xue, Z. Y. Liu, J. Huang, X. Q. Pan, Y. Huang, *J. Am. Chem. Soc.* **2018**, *140*, 9046–9050.
- [8] Y. H. Li, J. Xing, X. H. Yang, H. G. Yang, *Chem. Eur. J.* **2014**, *20*, 12377–12380.
- [9] M. Sarno, E. Ponticorvo, *Int. J. Hydrogen Energy* **2017**, *42*, 23631–23638.
- [10] X. Cheng, Y. H. Li, L. R. Zheng, Y. Yan, Y. F. Zhang, G. Chen, S. R. Sun, J. J. Zhang, *Energy Environ. Sci.* **2017**, *10*, 2450–2458.
- [11] J. Durst, A. Siebel, C. Simon, F. Hasché, J. Herranz, H. A. Gasteiger, *Energy Environ. Sci.* **2014**, *7*, 2255–2260.
- [12] R. Subbaraman, D. Tripkovic, D. Strmcnik, K.-C. Chang, M. Uchimura, A. P. Paulikas, V. Stamenkovic, N. M. Markovic, *Science* **2011**, *334*, 1256–1260.
- [13] L. Hui, Y. Xue, H. Yu, Y. Liu, Y. Fang, C. Xing, B. Huang, Y. Li, *J. Am. Chem. Soc.* **2019**, *141*, 10677–10683.
- [14] Y. Xue, L. Hui, H. Yu, Y. Liu, Y. Fang, B. Huang, Y. Zhao, Z. Li, Y. Li, *Nat. Commun.* **2019**, *10*, 2281.
- [15] Y. Xue, B. Huang, Y. Yi, Y. Guo, Z. Zuo, Y. Li, Z. Jia, H. Liu, Y. Li, *Nat. Commun.* **2018**, *9*, 1460.
- [16] P. Xiao, Y. Zhao, T. Wang, Y. Zhan, H. Wang, J. Li, A. Thomas, J. Zhu, *Chem. Eur. J.* **2014**, *20*, 2872–2878.
- [17] Y. Gong, M. Li, H. Li, Y. Wang, *Green Chem.* **2015**, *17*, 715–736.
- [18] W. A. Spieker, J. Liu, J. T. Miller, A. J. Kropf, J. R. Regalbutto, *Appl. Catal. A* **2002**, *232*, 219–235.
- [19] K. Hindmarsh, D. A. House, R. van Eldik, *Inorg. Chim. Acta* **1998**, *278*, 32–42.
- [20] B. L. He, Y. Ha, H. F. Liu, K. M. Wang, K. Y. Liew, *J. Colloid Interface Sci.* **2007**, *308*, 105–111.
- [21] W. Westwood, C. Bennewitz, *J. Appl. Phys.* **1974**, *45*, 2313–2315.
- [22] S. Siegel, H. R. Hoeskstra, B. S. Tani, *J. Inorg. Nucl. Chem.* **1969**, *31*, 3803–3807.
- [23] A. Lazauskas, J. Baltrusaitis, L. Puodziukynas, M. Andrulevicius, G. Bagdziunas, D. Volyniuk, S. Meskinis, G. Niaura, T. Tamulevicius, V. Jankauskaite, *Carbon* **2016**, *107*, 415–425.
- [24] M. Peuckert, F. P. Coenen, H. P. Bonzel, *Electrochim. Acta* **1984**, *29*, 1305–1314.
- [25] H. Karhu, A. Kalantar, I. J. Väyrynen, T. Salmi, D. Y. Murzin, *Appl. Catal. A* **2003**, *247*, 283–294.
- [26] Z. Q. Wang, X. Ren, X. F. Shi, A. M. Asiri, L. Wang, X. N. Li, X. P. Sun, Q. J. Zhang, H. J. Wang, *J. Mater. Chem. A* **2018**, *6*, 3864–3868.
- [27] D. A. Svintsitskiy, L. S. Kibis, A. I. Stadnichenko, S. V. Koscheev, V. I. Zai-kovskii, A. I. Boronin, *ChemPhysChem* **2015**, *16*, 3318–3324.
- [28] A. Thomas, A. Fischer, F. Goettmann, M. Antonietti, J.-O. Müller, R. Schlögl, J. M. Carlsson, *J. Mater. Chem.* **2008**, *18*, 4893–4908.
- [29] J. H. Liu, T. K. Zhang, Z. C. Wang, G. Dawson, W. Chen, *J. Mater. Chem.* **2011**, *21*, 14398–14401.
- [30] J. H. Thurston, N. M. Hunter, L. J. Wayment, K. A. Cornell, *J. Colloid Interface Sci.* **2017**, *505*, 910–918.
- [31] L. Chen, Y. Peng, J.-E. Lu, N. Wang, P. Hu, B. Lu, S. Chen, *Int. J. Hydrogen Energy* **2017**, *42*, 29192–29200.
- [32] M. Ahmadi, H. Mistry, B. Roldan Cuenya, *J. Phys. Chem. Lett.* **2016**, *7*, 3519–3533.
- [33] C. H. Booth, R-Space X-ray Absorption Package, **2010**, see: <http://lisse.lbl.gov/RXAP/>.
- [34] J. A. Horsley, *J. Chem. Phys.* **1982**, *76*, 1451–1458.
- [35] A. N. Mansour, J. W. Cook, D. E. Sayers, *J. Phys. Chem.* **1984**, *88*, 2330–2334.
- [36] D. Friebe, D. J. Miller, C. P. O’Grady, T. Anniyev, J. Bargar, U. Bergmann, H. Ogasawara, K. T. Wikfeldt, L. G. M. Pettersson, A. Nilsson, *Phys. Chem. Chem. Phys.* **2011**, *13*, 262–266.

- [37] H. Yoshida, S. Nonoyama, Y. Yazawa, T. Hattori, *Phys. Script.* **2005**, T115, 813–815.
- [38] <https://materialsproject.org/materials/mp-7868/>.
- [39] M. R. Gao, Z. Y. Lin, J. Jiang, C. H. Cui, Y. R. Zheng, S. H. Yu, *Chem. Eur. J.* **2012**, 18, 8423–8429.
- [40] A. L. Ankudinov, J. J. Rehr, *Phys. Rev. B* **1997**, 56, R1712–R1716.
- [41] Y. Peng, W. Z. Pan, N. Wang, J. E. Lu, S. W. Chen, *ChemSusChem* **2018**, 11, 130–136.

Manuscript received: October 5, 2019

Accepted manuscript online: October 28, 2019

Version of record online: December 10, 2019